Depressurization of CO_2 in a pipe: High-resolution pressure and temperature data and comparison with model predictions

Svend Tollak Munkejord[*], Anders Austegard, Han Deng, Morten Hammer, H. G. Jacob Stang, Sigurd W. Løvseth

SINTEF Energy Research, P.O. Box 4761 Torgarden, NO-7465 Trondheim, Norway

Abstract

The design of safe and cost-efficient CO_2-transportation systems is an integral part of CO_2 capture and storage (CCS) deployment. To achieve this, accurate transient flow models capturing the occurrence of gas, liquid and solid CO_2 are needed. These in turn rely on experimental validation. In this work, we present a new experimental facility designed to capture pressure and temperature during the depressurization of CO_2 and CO_2-rich mixtures in a tube at high spatial and temporal resolution. Experiments with pure CO_2 starting from both gaseous and dense (liquid) states are presented, and a reference experiment with N_2 is included. The experimental results for both pressure and temperature are analysed by comparison with predictions by a homogeneous equilibrium model. Emphasis is put on the decompression-wave speed, of particular relevance for running-ductile fracture in CO_2-transportation pipelines. We observe good agreement with predicted decompression-wave speeds in the single-phase region, and fair agreement for two-phase flows when the calculations are based on the assumption of equilibrium. However, the observed 'pressure plateau', a key factor in the prediction of running-ductile fracture, can be significantly lower than that calculated assuming equilibrium.

Keywords: carbon dioxide, depressurization, decompression, experiment, CFD, fluid dynamics, thermodynamics

1. Introduction

CO_2 capture and storage (CCS) is recognized as one of the means that are necessary to mitigate climate change (Edenhofer *et al.*, 2014). This is true both in a transition period as the use of fossil fuels is reduced, and more permanently, to mitigate emissions inherent in industrial processes (Voldsund *et al.*, 2019). Therefore, by the mid century, each year, several gigatonnes of CO_2 will have to be transported from the capture plants to the storage sites (IEA, 2017). In order to design, optimize and operate CO_2-transportation and injection systems in a safe and efficient way, engineers will need to quantify processes and phenomena that may not be readily covered by existing engineering tools (Munkejord *et al.*, 2016).

---

[*]Corresponding author.
Email address: `svend.t.munkejord [a] sintef.no` (Svend Tollak Munkejord)

One of those processes is the depressurization of pipes, which is relevant to several safety and operational aspects, involving running-ductile fracture, transient flow and temperature variation, as pointed out in the following. Data and models for pipe depressurization are also employed to describe the upstream boundary condition for safety studies of the release and dispersion of CO_2 in the terrain (see the review by Pham and Rusli, 2016).

Pipelines transporting highly pressurized compressible fluids need to be designed to avoid running-ductile fracture (RDF) for more than 1–2 pipe sections (DNV, 2012). RDF is a phenomenon whereby a defect in the pipeline, caused by e.g. corrosion or external forces, develops into a fracture running along the pipe, sustained by the pressure forces from the escaping fluid. The most commonly used design method to assess RDF, the Battelle two-curve method (Maxey, 1974) is semi-empirical and was developed for natural gas. It turns out it is non-conservative for CO_2 (Jones *et al.*, 2013), presumably since it does not include the relevant physical phenomena (Aursand *et al.*, 2016a). The development of physics-based models describing running-ductile fracture requires validation not only on the top level, by full-scale tests (Cosham *et al.*, 2014, 2016; Di Biagio *et al.*, 2017; Michal *et al.*, 2018), but equally important, on the level of each of the sub-models, encompassing material mechanics, fracture mechanics, thermodynamics and fluid dynamics. The latter involves decompression-wave velocities and the pressure at which bubbles start developing in the liquid CO_2 – the accurate observation of which is one of the main contributions of this paper. The aforementioned pressure is often called 'saturation pressure' in the literature on running-ductile fracture. This denomination may cause misunderstanding, since it implies thermodynamic equilibrium, which, as we shall see, may not be established in the fast processes under study.

Pipe-depressurization experiments can also serve more generally to validate transient flow models. Indeed, the experimentally observed pressure-propagation speeds can be compared to those inherent in the fluid-dynamics model, and they can therefore aid in the selection of the appropriate mathematical formulation (see Munkejord *et al.*, 2016, and the references therein). For long-distance transportation in pipelines, the CO_2 will generally be compressed to a dense or liquid state. During decompression from such a state, there will be significant expansion and evaporative cooling. It is of interest to estimate the temperatures occurring, in order to determine whether there is a risk for materials to turn brittle, or for excessive thermal stresses to occur (Aursand *et al.*, 2017). To calculate these temperatures requires not only thermodynamics, but also heat-transfer models, a subject having received less attention so far in the context of CO_2 transportation. To validate such models, accurate temperature measurements are needed, and this constitutes the second main contribution of the present work.

As summarized in Munkejord *et al.* (2016), depressurization experiments in pipes and tubes were published by Armstrong and Allason (2014); Botros *et al.* (2013); Brown *et al.* (2013, 2014); Clausen *et al.* (2012); Cosham *et al.* (2012a); Drescher *et al.* (2014); Jie *et al.* (2012). Later, Guo *et al.* (2016, 2017); Yan *et al.* (2018) studied the depressurization of a large pipe of length 257 m and inner diameter 233 mm with full-bore opening and two orifices. They observed pressure transients attributed to phase change as pressure waves were reflected at the pipe ends. Cao *et al.* (2018) reported on temperature evolution and heat transfer in the experiments first presented by Guo *et al.* (2017). In particular, dry-ice formation was observed in the pipe during full-bore release from a dense-phase state. Teng *et al.* (2016) performed decompression experiments in a pipe of length 70 m and internal diameter 25 mm, focusing on the decompression-wave speed in cases without phase transfer. Gu *et al.* (2019) reported decompression experiments in a tube of length 14.85 m and internal diameter

15 mm, for different nozzle sizes in the millimetre range, studying the effect of N_2 as an impurity.

In a series of papers, Botros *et al.* (2016, 2017a,c,b) presented depressurization experiments of CO_2 and CO_2-rich mixtures in a tube of length 42 m and internal diameter 38.1 mm. The pressure measurements were accurate and of high resolution, allowing the decompression-wave speed to be calculated. However, no temperature data were provided.

Part of the studies on depressurization of CO_2 in pipes so far focuses on a semi-qualitative understanding of the phenomena. This means that although the data can be used for model validation, they may not be detailed or accurate enough for model development. Therefore, there is still a need for accurate pressure and temperature data with high resolution both in time and space. In the present work, therefore, we have constructed a new depressurization laboratory facility, part of the European CCS Laboratory Infrastructure (ECCSEL) (ECCSEL, 2020). It is densely and accurately instrumented, and has as a main purpose to publish high-quality datasets. Access for external researchers can also be obtained. The facility has been constructed to accommodate a wide range of CO_2-rich mixtures, and emphasis has been put on obtaining high-resolution and synchronized pressure and temperature data.

The three main contributions of this article are thus:

1. We present new depressurization experiments for CO_2 in a tube. Accurate and dense measurements of pressure and – for the first time – temperature are reported.
2. The data can be downloaded from Zenodo (Munkejord *et al.*, 2020). To our knowledge, this is the first time that this type of dataset is made openly available.
3. The experimental data are compared to calculations performed using a homogeneous equilibrium model (HEM), which is well known and well defined. This allows interpretation and discussion of the results on the basis of a firm reference.

The rest of this article is organized as follows. Section 2 describes the experimental facility. The employed HEM is briefly referenced in Section 3. The results are presented and discussed in Section 4, and Section 5 concludes the article.

2. Experimental set-up and methodology

This section describes the experimental set-up. Section 2.1 gives an overview of the ECCSEL depressurization facility, while the instrumentation is described in Section 2.2. An overview of the experimental procedure is provided in Section 2.3, and the experimental uncertainties are discussed in Section 2.4.

The experimental facility is located at the roof of the Thermal Engineering Laboratories at the campus of the Norwegian University of Science and Technology in Trondheim. The construction and operation of the facility has been extensively analysed with respect to health, safety and the environment. In particular, analyses including computational fluid dynamics (CFD) have been carried out to ascertain that the operation of the facility would not lead to elevated CO_2 levels at the street level. This has been confirmed by CO_2-concentration measurements during the first experiments.

2.1. ECCSEL depressurization facility

The ECCSEL depressurization facility has been constructed to provide highly accurate data for fast decompression of pure CO_2 and CO_2-rich mixtures in a tube. Figure 1a gives an overview of the facility, which consists of a test section with heating

(a) System (RV: relief valve; OV: one-way valve; PV: pneumatic valve)

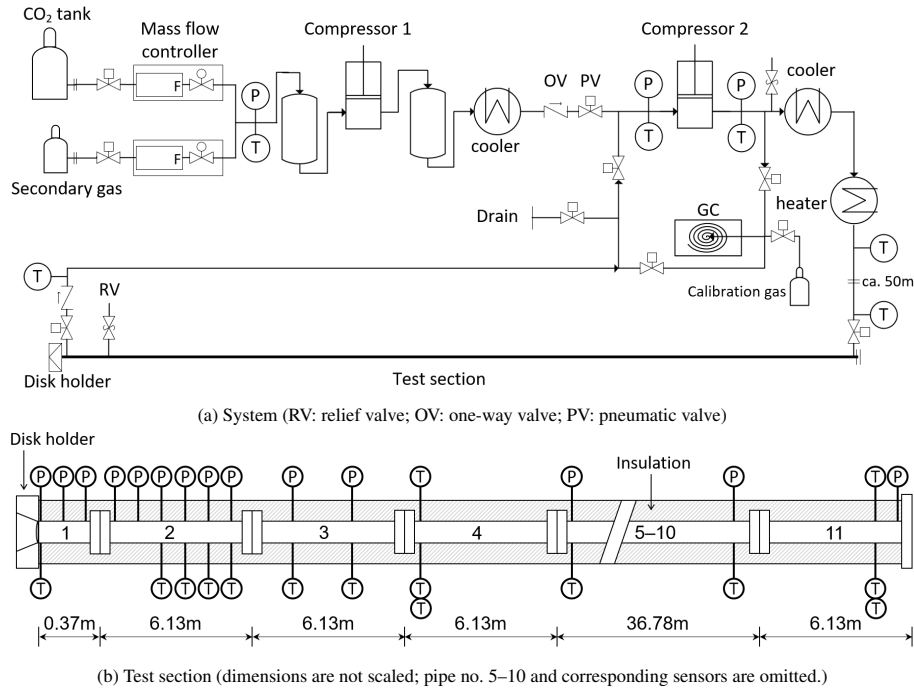(b) Test section (dimensions are not scaled; pipe no. 5–10 and corresponding sensors are omitted.)

Figure 1: Schematic of the ECCSEL depressurization facility.

Table 1: Density and thermal properties of the test section materials.

	Density ($kg\,m^{-3}$)	Thermal conductivity ($W\,m^{-1}\,K^{-1}$)	Specific heat ($J\,kg^{-1}\,K^{-1}$)
Pipe steel	8000	15	500
Insulation layer	75	0.032	840

elements, a rupture device, a gas supply system, two-stage compression with a cooling aggregate, and a heater. Figure 2 shows a photograph of the depressurization tube (test section). At one point it is anchored horizontally to the railings by L profiles. This arrangement is solid, but has some flexibility.

The operating pressure of the facility is up to 20 MPa, and the operating temperature is between 5 °C and 40 °C. The test section is made of 11 stainless steel (SS316, EN 1.4401) pipes of inner diameter 40.8 mm and outer diameter 48.3 mm, which give a total length of 61.67 m, as illustrated in Figure 1b. The internal surface of the pipes were honed to a mean roughness (roughness average), R_a, ranging from 0.2 μm to 0.3 μm. To achieve a uniform axial temperature, the tube is wrapped by heating cables of type PTC, whose resistance increases with temperature to avoid overheating. The heating cables give a power output of 1900 W at 20 °C and 950 W at 40 °C. The tube with heating elements is insulated by a 60 mm thick glass wool layer. The whole test section is covered by a stainless-steel mantle of diameter 190 mm. The thermal properties of the pipe and insulation layer are given in Table 1.

The rupture device consists of an X-scored rupture disk and a disk holder. Rupture disks of type Fike SCRD BT FSR with a specified burst pressure 110 barg and 120 barg at 22 °C are used for the current tests, with a burst tolerance of ±5%. Once the disk

4

Figure 2: The ECCSEL depressurization tube. The CO_2 is vented through the stack in the background. The container at the left contains support equipment.

ruptures, the depressurization is triggered. The disk holder has an inner diameter of 63 mm and the open membrane area of the rupture disk matches the disk holder, which gives a larger opening area than the cross-section area of the tube, to ensure choking at the end flange. An example of a disk before and after rupture is shown in Figure 3. For commissioning tests at low pressure with gas, plastic disks were used.

The test section is connected to a system for gas supply and compression. CO_2 and secondary gases are supplied by separate pipelines connected to corresponding gas cylinders. For tests with mixtures, the desired composition is achieved by the two Bronkhorst mass-flow controllers. Two stages of compression with cooling are used to build up the pressure in the test section and attain the desired experimental condition. The two compressors are of type Maximator Gas Booster DLE 5 and DLE 15. The heater is used to regulate the temperature at the inlet of the test section. A return pipeline is for circulation to achieve uniform temperature and composition in the case of mixtures. A micro gas chromatograph (GC) is connected for measuring the mixture composition, by taking samples from upstream of the pipe inlet and downstream of the

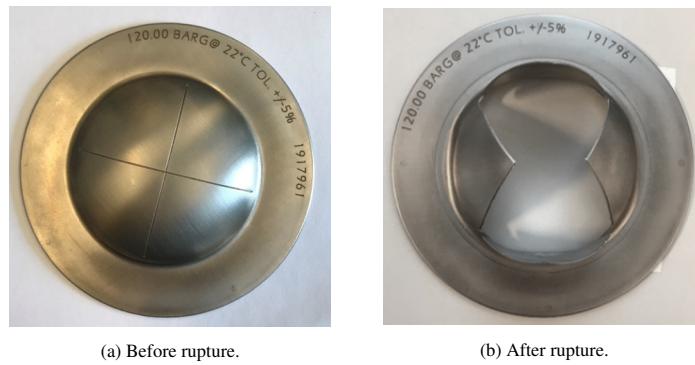(a) Before rupture.   (b) After rupture.

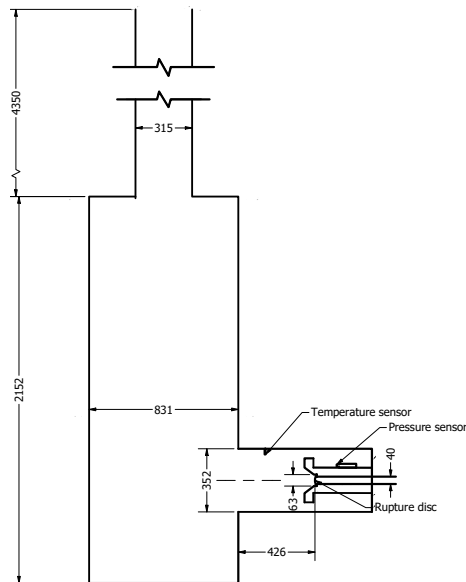Figure 3: Rupture disk from Test no. 8.

Figure 4: Main dimensions (mm) of the vent stack connected to the test facility, centre cross-section view.

pipe outlet. Pressure-relief valves are installed after the second compressor and at pipe no. 2, which open at a pressure of 20 MPa. The drain lines (not shown in the figure for simplicity) are used for emptying the system after each test while a vacuum pump is installed on the same line for evacuating the system before each test.

The vent stack has been installed in order to reduce the noise from the experiments and to reduce the CO_2 concentration on street level. It has been designed in order not to influence the experimental conditions upstream. In particular, the minimum diameter is 8 times larger than the tube inner diameter. The negligible influence of the vent stack on the experiments is confirmed by pressure recordings inside the stack. The main dimensions of the vent stack can be seen in Figure 4.

2.2. Instrumentation

The test section is specifically instrumented to capture decompression waves. Sixteen fast-response pressure transducers are flush mounted to the internal surface along

6

(a) Side-mounted pressure sensor.

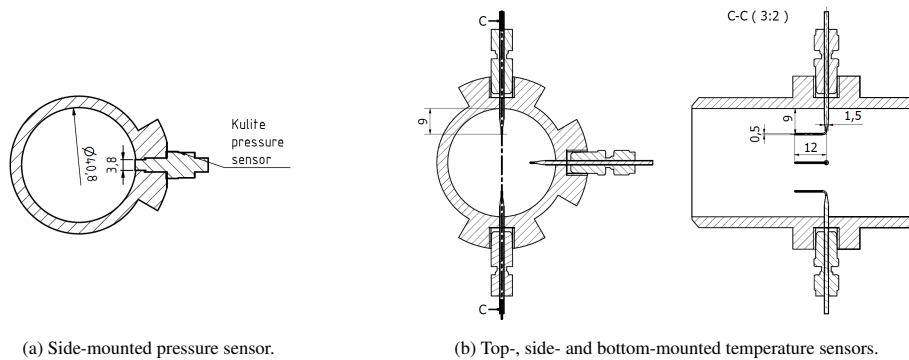(b) Top-, side- and bottom-mounted temperature sensors.

Figure 5: Installation of pressure and temperature sensors. Dimensions in mm.

the pipe with dense distribution close to the rupture disk, as illustrated in Figure 1b. The pressure transducers are side mounted as illustrated in Figure 5a. The transducers are of type Kulite CTL-190(M), with a full-scale (FS) pressure of 20 MPa and operating temperature down to $-196\,°C$. They have a bandwidth up to 200 kHz and an accuracy of 0.5% of the FS pressure. The pressure sensors are calibrated before and after the depressurization in each experiment with a Keller pressure transmitter of type PAA-33X located after the second compressor in Figure 1a. It has an FS pressure of 30 MPa and an error band of 0.05%. The pressure-measurement uncertainty is estimated in Section 2.4.1.

A total of 23 Type E thermocouples are installed for the measurement of the fluid temperature, among which 11 are placed at axial positions together with pressure sensors on opposite sides of the pipe. The remaining 12 thermocouples are installed at the top, bottom and side of the pipe at four locations in order to capture any stratification of the flow, as depicted in Figure 5b. The Type E thermocouples are calibrated against two Ultra Precise RTD (resistance temperature detector) sensors of diameter 3 mm with converter Omega PT-104A, located at the inlet and outlet of the test section as shown in Figure 1a. The two RTD sensors are of 1/10 DIN accuracy, which corresponds to an accuracy of $±0.04\,K$ at $20\,°C$. The calibration of thermocouples is performed with 20 measurement points in the two-phase CO_2 region and gives an uncertainty of $±0.22\,°C$. The locations of all the pressure and temperature sensors on the test section are listed in Table 2.

A National Instruments PXIe-1085 Chassis is used for data acquisition, with two PXIe-4492 cards for signal acquisition from the fast-response pressure sensors and one PXIe-4302 card for the thermocouples. The three PXIe cards are locked to a common reference clock. The data from the pressure and temperature sensors are logged at 100 kHz and 1 kHz, respectively, which gives a pressure-data resolution of 10 μs and a temperature-data resolution of 1 ms. The high-frequency data are stored for 9 s, including about 0.3 s before disk rupture and 8.7 s after the rupture. This is accomplished by storing the data for 0.3 s in the computer and registering when detecting a sudden pressure drop. After this period, both pressure and temperature are collected at 50 Hz.

The high-frequency logging data are filtered after the fast pressure drop for plots and calculations of wave speed at low pressure. The criterion is to keep all the essential information. For each test, the reported initial conditions are based on data from about 0.5 ms to 1 ms before disk rupture, using the average of the measurements by all the pressure transducers and the length-weighted average of the measurements by the ther-

7

Table 2: Locations of pressure and temperature sensors at 25 °C.

Distance from open end (m)	Pressure sensor	Temperature sensor (side)	Temperature sensor (bottom, side, top)
0.080	PT201	TT201	
0.180	PT202		
0.280	PT203		
0.484	PT204		
0.800	PT205		
1.599	PT206	TT206	
3.198	PT207	TT207	
4.798	PT208	TT208	
6.397	PT209	TT209	
7.996	PT210	TT210	
9.595	PT211	TT211	
15.292			TT241, TT242, TT243
19.990	PT212	TT212	
29.986	PT213	TT213	
30.686			TT251, TT252, TT253
39.984	PT214	TT214	
46.085			TT261, TT262, TT263
49.982	PT215	TT215	
61.280			TT271, TT272, TT273
61.479	PT216		

Table 3: Summary of specifications and instrumentation of test section.

Parameter	Value
Pipe inner diameter	40.8±0.4 mm
Pipe outer diameter	48.3 mm
Pipe length	61.668 m at 25 °C
Pipe mean roughness (R_a)	0.2–0.3 μm
Insulation thickness	60 mm
Pressure transducers	16 units, high frequency data 100 kHz
Thermocouples	23 units, high frequency data 1 kHz

mocouples at the side of the pipe. The instrumentation together with the specifications of the test section are summarized in Table 3.

2.3. Experimental procedure

The experimental procedure mainly consists of the following steps. First, the rupture disk is installed and the system is evacuated. Then the test section is filled with CO_2 while pressure is build-up. When the pressure in the test section reaches about 70% of the desired pressure, circulation is started in order to achieve a uniform temperature. The temperature is controlled using heating elements. The desired pressure and temperature are achieved by further heating and addition of CO_2 if needed, both at a controlled rate, until the disk ruptures. Upon disk rupture, the two pneumatic valves at the end of the test section are automatically closed to stop circulation. After the test, the system is emptied.

2.4. Uncertainty analysis

Having described the test facility and instrumentation, in this section, we further discuss uncertainty in the pressure measurement, temperature measurement and in the
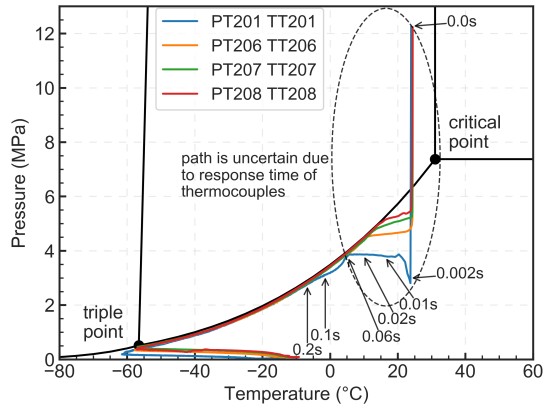
8

Figure 6: Depressurization path from Test no. 8 in a phase diagram drawn using the Span–Wagner EOS.

inferred wave speed. In this work, expanded and symmetric uncertainties with a confidence level of 95% are presented, which is identical to multiplying the standard uncertainty by a coverage factor of $k = 2$ for normally distributed data (Joint Committee for Guides in Metrology, 2008; Taylor and Kuyatt, 1994). That is, the real values are not further from the measurements than the stated uncertainty with 95% estimated probability.

2.4.1. Pressure measurement

The fast-response pressure transducers are calibrated before and after the depressurization in each experiment with the Keller pressure transmitter, having an uncertainty of 4.7 kPa resulting from calibration against a D&H deadweight tester. The interpolation points are selected at 3–4 pressure levels during the process of pressure building up. Additionally, one point at atmospheric pressure is included, when the depressurization is finished and the pressure and temperature in the pipe are stable.

To estimate the pressure-measurement uncertainty, we consider three components: the calibration uncertainty due to the uncertainty of the Keller sensor; the uncertainty due to the linear interpolation of calibration points (standard error of regression); and the uncertainty due to temperature variations in the pressure sensors after disk rupture. The linear interpolation gives an uncertainty about 40 kPa at high pressure levels. The output of the temperature sensors varies with temperature, and this gives an uncertainty about 44 kPa. The resulting total measurement uncertainty in pressure is estimated to 60 kPa.

2.4.2. Response time of thermocouples

The uncertainty in temperature measurement largely lies in the response time of the thermocouples. Figure 6 shows the depressurization path at four locations in Test no. 8 (see Section 4 for an overview of the tests). It can be seen that the path close to the outlet (PT201, TT201) passes and deviates from the liquid-gas saturation curve in the first 0.06 s.

We have estimated the response time by calculating the transient heat transfer from the fluid to the thermocouple sheath and further on to the core of the thermocouple. The result for Test 8 is a temperature-sensor response time of about 30 ms for the initial temperature drop. This indicates that the 'thermodynamic path' in Figure 6 is uncertain

9

Table 4: Number and position of pressure transducers used for calculation of wave speed.

Study	no. of PTs	normalized locations (L/D)	pipe roughness
Botros *et al.* (2007)	4	1.2 – 17.0	R_z[*] 1.0 μm
Botros *et al.* (2016)	5	0.77–9.19	R_z 0.635 μm
Cosham *et al.* (2012b)	18–20 at high pressure; 10–12 at low pressure	0.59 – 24.87 (18)/41.27 (20); 0.59 – 6.42 (10)/8.47 (12)	R_a 5 μm
Present	5 at high pressure; 3–5 at low pressure	1.96–19.61 (5) 1.96–6.86 (3)	R_a 0.2–0.3 μm

[*] Our interpretation.

in the marked region. Therefore, this plot, depending on temperature measurements, cannot say much about a possible departure from thermodynamic equilibrium in the experiments. However, as will be shown in Section 4.2, analyses depending only on the measured pressure can illustrate non-equilibrium effects during the first, rapid decompression.

2.4.3. Measured decompression-wave speed

The decompression-wave speed can be evaluated by considering the arrival time at the pressure sensors of decompression waves at given pressure levels. By linearly fitting the arrival times at different sensors as a function of their positions, we can estimate the wave speed. The selected pressure transducers should be within a short distance from the open end of the pipe to minimize the effect of friction. Meanwhile, the number of points should be sufficient to reduce the effect of slightly varying sensor performance. Table 4 shows the number and positions of pressure transducers used for the calculation of wave speed in several studies. In the present study, the first five pressure transducers are used for the calculation of the wave speed at high pressures (above the plateau, see Section 4.2). The number of points and distance to the open end of the pipe are within a reasonable range. Due to the honed inner surface, the pipe roughness is very low in the present study.

The estimation of uncertainty in the experimental wave speed, w, is performed by a method similar to that described by Botros *et al.* (2004); Botros (2010),

$$\frac{\delta w}{w} = \sqrt{\left(\frac{\delta L}{L}\right)^2 + \left(\frac{\delta t}{t}\right)^2}, \tag{1}$$

where L is the location of the sensors used in the calculation of wave speed and t is the time of signals. Similarly, we consider the uncertainty in wave-arrival time, δt,

$$\delta t = \delta t_1 + \delta t_2 + \delta t_3, \tag{2}$$

where δt_1 is the uncertainty due to data acquisition, δt_2 is the uncertainty due to the filtering, and δt_3 is the uncertainty due to uncertainty in pressure as $(\partial t/\partial P)\delta P$.

As an example, Table 5 lists components of the uncertainties at two pressures, one at a high pressure of 12 MPa without data filtering and the other at a low pressure of 3.5 MPa with data filtered by using the average value of every 200 points. It can be seen that at a pressure close to the initial pressure, the uncertainty is 1.7%, of which the uncertainty due to data acquisition is the major component. The wave travel time, t, between the first five sensors is quite small because of the fast decompression wave. At low pressure, the uncertainties from filtering and pressure measurement are predominant as $\partial t/\partial P$ becomes greater, yielding an uncertainty of 6.2%.

Table 5: Example of uncertainty in wave speed at two pressures from Test no. 8.

Quantity	Unit	Pressure 12 MPa	Pressure 3.5 MPa
Distance uncertainty, δL	mm	2	2
Distance, L, PT201–PT205	mm	720	720
Relative distance uncertainty, $\delta L/L$		0.00278	0.00278
Time, t, PT201–PT205	μs	1486.9	109443.7
Time uncertainty data acquisition, δt_1	μs	20	20
Time uncertainty filtering, δt_2	μs	0	154.8
Time uncertainty δt_3 due to uncertainty in pressure	μs	4.2	6608.8
Relative time uncertainty, $\delta t/t$		0.01628	0.06198
Wave-speed uncertainty, $\delta w/w$		0.0165	0.0620

3. Models

To facilitate the discussion of the experimental results to be presented in the following, we will compare with 1D CFD simulations. Here we will employ the homogeneous equilibrium model (HEM) discussed by Munkejord and Hammer (2015); Munkejord *et al.* (2016) and briefly summarized in the following. The model equations are discretized using the robust FORCE (first-order centred) scheme (Toro and Billett, 2000). We obtain a second-order method by employing a semi-discrete monotone upwind-centred scheme for conservation laws (MUSCL) along with a second-order strong-stability-preserving Runge-Kutta method. See Hammer *et al.* (2013) for details. This method captures fast transients in a robust way. For two-phase flow, the phases are assumed to be in mechanical, kinetic, thermal and chemical equilibrium at all times. For CO_2, we employ the equation of state (EOS) of Span and Wagner (1996), including a method to capture the formation of solid CO_2 as described in Hammer *et al.* (2013). For N_2 we use the Peng and Robinson (1976) equation of state from our in-house thermodynamics library (Wilhelmsen *et al.* (2017)).

The heat conduction through the pipe steel and the surrounding insulation is calculated by solving the heat equation in the radial direction in a two-layer domain, as described by Aursand *et al.* (2017). The in-tube heat-transfer coefficient is calculated based on the Dittus-Boelter correlation for forced convection (see Bejan, 1993, Chap. 6). Enhanced heat transfer due to boiling is accounted for by employing the correlation of Gungor and Winterton (1987). The outside heat-transfer coefficient is estimated to be $4\,\mathrm{W\,m^{-2}\,K^{-1}}$. The wall friction is calculated by the Friedel (1979) correlation.

For the present calculations, we employed a Courant-Friedrichs-Lewy (CFL) number of 0.85. For calculations below about 1 s, the calculations were performed on a spatial grid of 4800 cells, whereas for longer times, 1200 cells were used.

4. Results and discussion

The initial conditions of the depressurization experiments considered in this study are listed in Table 6. For convenience, the figures in this paper containing data from the tests are listed. Four experiments have been conducted with pure CO_2, three from a dense state and one from a gaseous state. One experiment has been conducted with N_2 in order to provide data without phase transfer as a complicating factor.

Table 6: Experimental conditions of the depressurization tests.

Test no.	Fluid	Pressure (MPa)	Temperature (°C)	Ambient temp. (°C)	Figures
3	CO_2	4.04	10.2	4	13
4	CO_2	12.54	21.1	22	8
6	CO_2	10.40	40.0	6	9, 14, 17, 18
8	CO_2	12.22	24.6	9	11, 15, 19, 20
11	N_2	5.13	10.0	9	7, 16
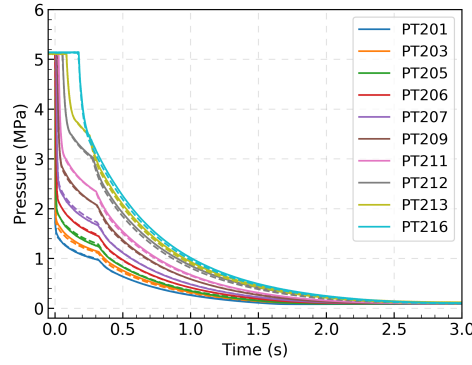
(a) Measured (full lines) and simulated (dashed lines) pressure at the sensor positions. Some sensors are omitted for readability.
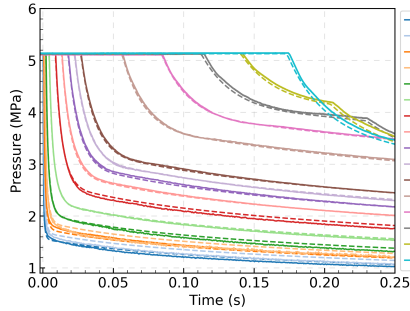
(b) Measured (full lines) and simulated (dashed lines) pressure at the sensor positions (zoom).
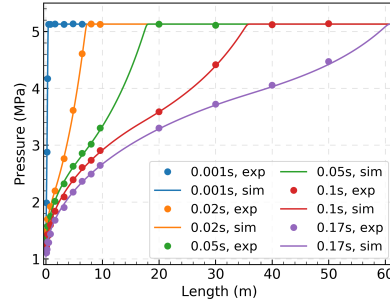
(c) Measured (dots) and simulated (full lines) pressure along the pipe.

Figure 7: Measured and simulated pressure for Test no. 11 (N_2).

4.1. Pressure

We first consider experiment no. 11, in which N_2 was depressurized from an initial state of 5.13 MPa and 10.0 °C. Figure 7 shows measured and calculated pressure at the sensor positions (Figures 7a–7b) and along the pipe (Figure 7c). In this case, there is very good agreement between the simulations and measurements. The kinks in the pressure traces after about 0.18 s in Figure 7b are due to the reflection at the closed end of the pipe.

Two pure-CO_2 experiments (nos. 4 and 8) were conducted at similar conditions in order to check the repeatability of the experiments. The differences in initial conditions, 12.54 MPa vs. 12.22 MPa and 21.1 °C vs. 24.6 °C are due to the control system of the laboratory facility and tolerances of the rupture disks. Measured pressures from the two experiments are shown in Figure 8. It can be seen that the data are consistent, and
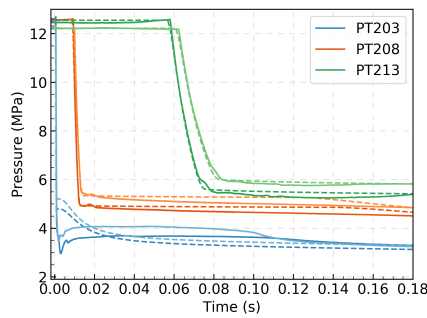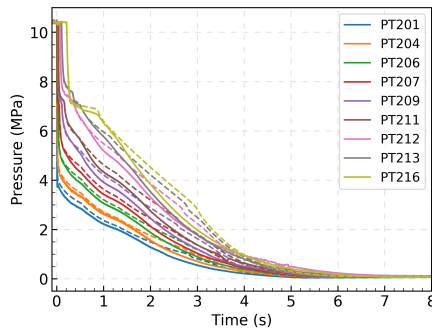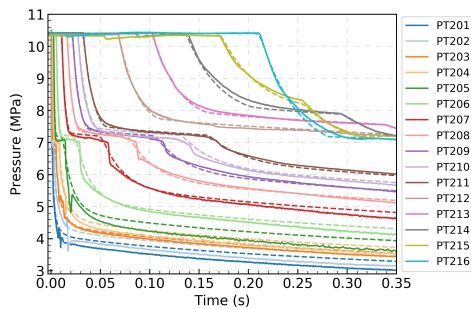
Figure 8: Measured (full lines) and simulated (dash lines) pressure for Test no. 4 (darker colours) and 8 (lighter colours).

the differences are explained by the differences in initial conditions.

Figure 9 shows measured and calculated pressure for Test no. 6, with an initial condition of 10.40 MPa and 40.0 °C for pure CO_2. The full duration is shown in Figure 9a, while Figure 9b concentrates on the fast initial transients. The pressure measurement traces (full lines) in Figure 9b reveal two different modes of pressure propagation. In the dense-phase region (elevated pressures in this case), the pressure waves are fast, while they are much slower in the two-phase region, below the critical pressure of

(a) Measured (full lines) and simulated (dashed lines) pressure at the sensor positions. Some sensors are omitted for readability.

(b) Measured (full lines) and simulated (dashed lines) pressure at the sensor positions (zoom).
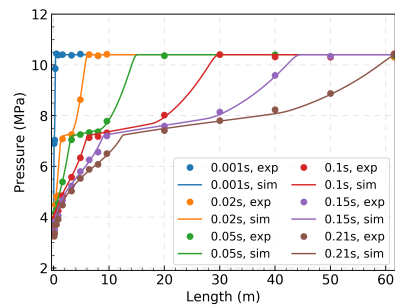
(c) Measured (dots) and simulated (full lines) pressure along the pipe.

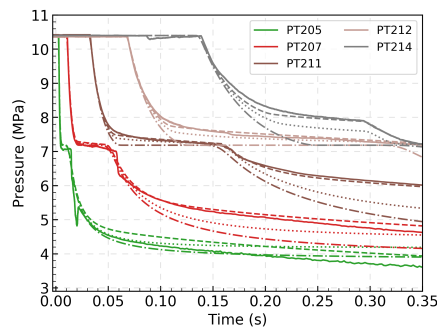Figure 9: Measured and simulated pressure for Test no. 6.

Figure 10: Pressure for Test no. 6: Effect of friction and heat transfer. Measured (full lines), simulated with heat and friction (dashed lines), simulated with only heat (dotted lines), simulated without heat and friction (dash-dotted lines).

7.38 MPa. Following a single pressure trace, one can observe that upon arrival of the first pressure wave, the pressure drops fast from about 10 MPa down to a 'plateau' pressure, which is close to the critical pressure in this case. Depending on the position, the pressure remains at the plateau for a while, after which it continues to decrease. One can observe that close to the outlet, the pressure drops fast also in the two-phase region.

In Figure9, pressures calculated using the homogeneous equilibrium model (HEM) are plotted along with the experimental values. As can be seen in Figure 9b, there is a tendency for the HEM to overestimate the two-phase pressure and the plateau pressure at positions close to the outlet. Otherwise, the agreement between the calculation and the experiment is, in our view, very good, particularly when considering the simplifications inherent in the HEM. The good agreement can also be seen for the pressure profiles plotted along the pipe in Figure 9c.

In Figure 9b, it can be observed that the 'plateau' pressure increases along the tube. The reason is friction and heat transfer, as illustrated in Figure 10. In the figure, we have plotted HEM simulation results where friction has been turned off (dotted lines). It can be seen that no friction gives lower plateau pressures, but they still increase along the tube. The figure also shows simulation results where both friction and heat transfer have been turned off. This gives a constant plateau level along the tube. A further observation can be made by considering the simulated pressures at position PT205, which is the farthest positioned sensor employed to calculate depressurization-wave speeds (see next section). According to the simulations, at this position, friction and heat transfer have a negligible influence on the pressure level until about 0.03 s, and this covers most of the depressurization wave-speed curve.

Results for Test no. 8 (12.22 MPa and 24.6 °C) are plotted in Figure 11. By comparing the pressure traces in Figure 9b with those in Figure 11b, we observe three main differences. First, the single-phase pressure-propagation speed is almost twice as high in the latter, due to the more liquid-like initial state (lower compressibility). Second, upon depressurization, the two-phase region is encountered at a lower pressure, around 5 MPa instead of around the critical pressure. Third, there are larger deviations between the measured and calculated pressure close to the outlet in the two-phase region. Here, the measured pressure drops rapidly and then levels off, whereas the calculated pressure decreases somewhat more gradually.
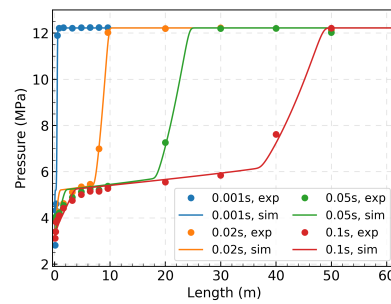
The difference between Test no. 6 and 8 is also illustrated by the difference in the

14
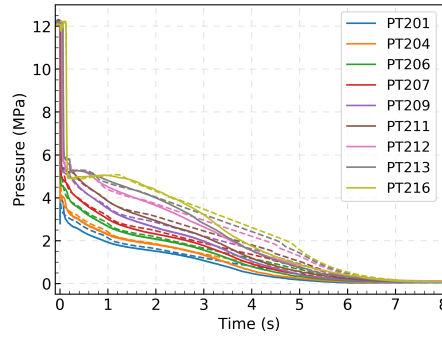
(a) Measured (full lines) pressure at the sensor positions.
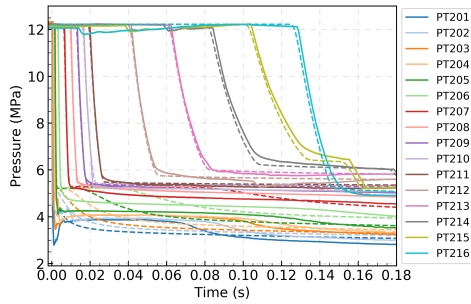
(b) Measured (full lines) and simulated (dashed lines) pressure at the sensor positions (zoom).

(c) Measured (dots) and simulated (full lines) pressure along the pipe.

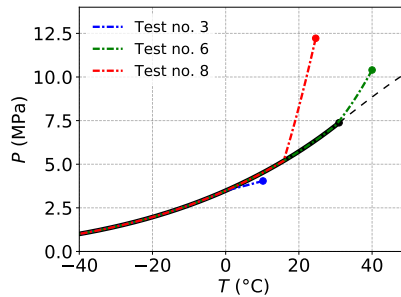Figure 11: Measured and simulated pressure for Test no. 8.

Figure 12: Saturation curve (black solid) for CO_2, with the extension (black dashed) where $\partial^2\rho/\partial P^2 = 0$ (at constant temperature), is plotted together with the isentropes of Test 3, 6 and 8.

speed of the initial decompression. For instance, at the first pressure sensor (PT201), for Test no. 6, it takes $230\,\mu s$ for the pressure to drop from the initial value to 7.07 MPa, whereas for Test no. 8, it takes $190\,\mu s$ for the pressure to drop from the initial value to 4.29 MPa.

The reason why Test 6 exhibits two-phase behaviour close to the critical point whereas Test 8 encounters the two-phase region at about 5 MPa is illustrated in Figure 12. Here the process paths have been drawn in the phase diagram assuming isentropic decompression and thermodynamic equilibrium. It can be seen that both Test 6 and 8 hit the two-phase line from the liquid side of the phase diagram. The main

factors determining the pressure at which two-phase flow is encountered, are the initial state and the form of the isentropes. The figure also shows that in Test 3, the two-phase line is encountered from the gas side. This is further discussed in the next section.

4.2. Decompression-wave speed

The decompression-wave speed is a main quantity in the assessment of running-ductile fracture in pipelines transporting pressurized fluids, see e.g. Aursand *et al.* (2016a) and the references therein. Further, by comparing measured decompression-wave speeds by those predicted by models, we can assess the suitability of those models to predict rapid transients in compressible fluids. The measured pressure traces presented in the previous section can be employed to obtain the decompression-wave speed, e.g., by using a procedure similar to the one described by Botros *et al.* (2007, 2010, 2016). The depressurization-wave speed is determined as the slope of the linear fit of the locations and wave arrival time of the first five pressure transducers.

If we assume one-dimensional isentropic flow, we can calculate the decompression-wave speed for a fully-developed wave at a given pressure level, p, along the isentrope, by

$$v(p) = c(p) - \int_p^{p_i} \frac{1}{\rho(p')c(p')} \, \mathrm{d}p', \tag{3}$$

where c is the speed of sound and p_i is the initial pressure, as discussed by Aursand *et al.* (2016a). For two-phase states, full equilibrium is often assumed. This amounts to what is usually done in the 'two-curve method', see e.g. Aursand *et al.* (2016a). In the following, we will also present calculations where no phase transfer is assumed, i.e., the fluid remains in a meta-stable state.

The expression (3) is evaluated using an equation of state (EOS). Hence, at least for single-phase states, comparing experimentally determined wave speeds with those calculated using (3), will constitute a good test of the EOS. We employ the Span–Wagner EOS for CO_2 and the Peng–Robinson EOS for N_2.

Figure 13 shows the experimentally determined wave speed, along with ones calculated using (3), for Test no. 3. Two assumptions have been made; full equilibrium (blue line) and no phase transfer (green line). This means that the green line represents the wave speed for a fluid that remains a (sub-cooled) gas. It is interesting to note that although the initial state is gaseous, the isentropic decompression brings the state into the two-phase region (see Figure 12). This indicates that the state is a subcooled gas below about 3.5 MPa, and that droplets start forming at about 2.8 MPa. There is good agreement with the analytical single-phase model above 3.5 MPa and with the analytical full-equilibrium model below 2.8 MPa.

The measured and the calculated decompression wave speed for Test no. 6 are shown in Figure 14. Here, the fluid is initially in a supercritical state, which leads to a large discontinuity in the wave speed at the phase boundary. As the dense phase turns into two-phase gas-liquid, the wave speed drops from about $170 \, \mathrm{m \, s^{-1}}$ to about $60 \, \mathrm{m \, s^{-1}}$. In this case, it was challenging to plot all of the pressure-wave-speed curve, since the measured pressure was not monotonous in the two-phase region, see Figure 9b. The dotted line is a straight line connecting the values extracted from the measurements. In the graph, the blue line represents the wave speed calculated using (3) while assuming full equilibrium. The green line is plotted for a meta-stable liquid state. This line ends at the point where the isentrope reaches the spinodal. It can be observed that this calculation, representing the highest degree of thermodynamic non-equilibrium, yields a lower pressure than the equilibrium calculation. It can be seen that the experimental data lie between the two.
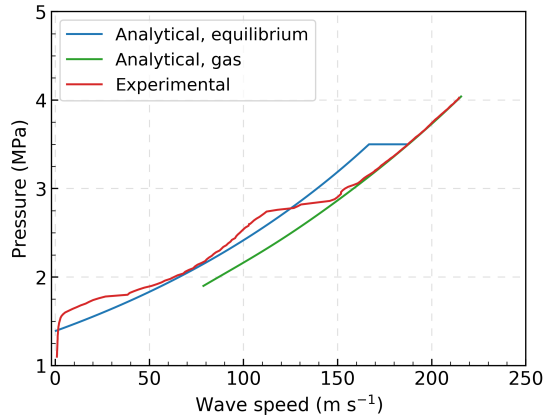
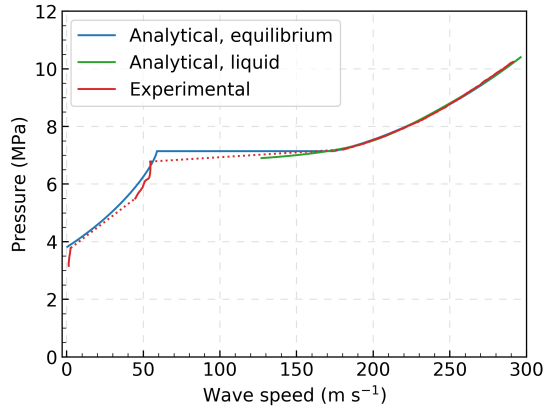Figure 13: Measured and calculated wave speed for Test no. 3.

Figure 14: Measured and calculated wave speed for Test no. 6.

We remark that the calculations shown in Figure 14 have been performed using a temperature of 39.5 °C, which is the initial average temperature at the positions of the pressure sensors involved. This temperature is 0.5 K lower than the initial average temperature of the test section as a whole.

In Figure 15, we have plotted the wave speed for Test no. 8. As was seen for Figure 11b, it can be observed that the initial wave speed, at 12 MPa, is high in this case, at about 480 m s^{-1}. As the phase boundary is encountered, at about 5.2 MPa, the wave speed drops from about 370 m s^{-1} to below 40 m s^{-1}, at least according to the model (3).

In this case we have been able to plot a larger part of the experimental wave speed, by using output from different sensors. It can be observed that while the full-equilibrium model (3) predicts a sharp kink at the transition between the single-phase and the two-phase region at 370 m s^{-1}, the experiment indicates that the transition is smoother. The experiment also indicates that the pressure goes significantly below the equilibrium (boiling) pressure. This is consistent with the hypothesis that due to the rapid process, we do not have full thermodynamic equilibrium, illustrated by the green line for a meta-stable liquid state. This indicates that in the experiment, we observe a
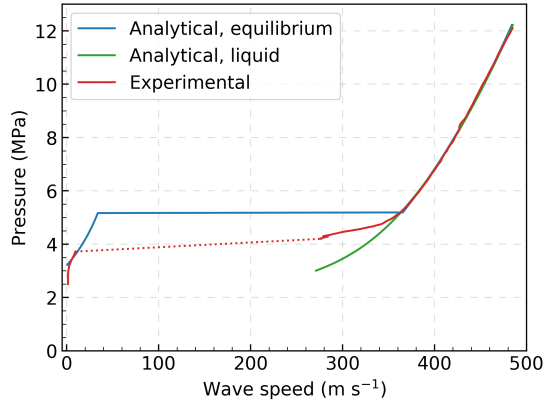
17

Figure 15: Measured and calculated wave speed for Test no. 8.

certain degree of non-equilibrium. To quantify this constitutes an interesting avenue for further research. We observe that in Test no. 8, there is a larger difference between the experimental data and the full-equilibrium calculation than for Test no. 6 in Figure 14. We hypothesize that this is because in Test no. 8, the state is farther from the critical point, with a lower compressibility yielding a faster decompression process. Further, the nucleation barrier calculated using classical nucleation theory is a strong function of surface tension (Aursand *et al.*, 2016b). When the state approaches the critical point, the surface tension approaches zero, the nucleation barrier vanishes, and the phase transition commences at lower sub-cooling and at a higher rate.

We note that a similar observation was made by Botros *et al.* (2016). For their tests with a supercritical initial state, there was fair agreement between the observed plateau pressure and that predicted with the full-equilibrium assumption, whereas for their test with a dense liquid initial state, the measured plateau pressure was significantly lower than the predicted one. These results support the observation by Cosham *et al.* (2012a) that for running-ductile fracture assessments, it is conservative to employ the saturation pressure.

4.3. Temperature

In the present study, we have emphasized temperature measurements, since, during depressurizations, low temperatures may be attained, which may render certain materials brittle. Further, the temperature measurements give indications regarding flow regime and solid-CO_2 formation.

We first consider the pure-N_2 Test no. 11, where measured and simulated temperatures are plotted as a function of time at four positions in Figure 16. We observe excellent agreement between measurements and simulation near the outlet (Figures 16a and 16b). As we approach the closed end (Figure 16c), the cooling phase of the experiment is very well reproduced by the model, but during the re-heating phase, the temperature is overpredicted by 5 °C to 10 °C. At the closed end (Figure 16d) of the pipe, we make two observations. First, the measured temperature gets as low as −78 °C. Second, at this point, the model severely underpredicts the temperature, down to −150 °C. The probable cause of this is the fact that we employ an in-tube heat-transfer correlation for forced convection, which is likely to underpredict the heat-transfer coefficient for low flow velocities.
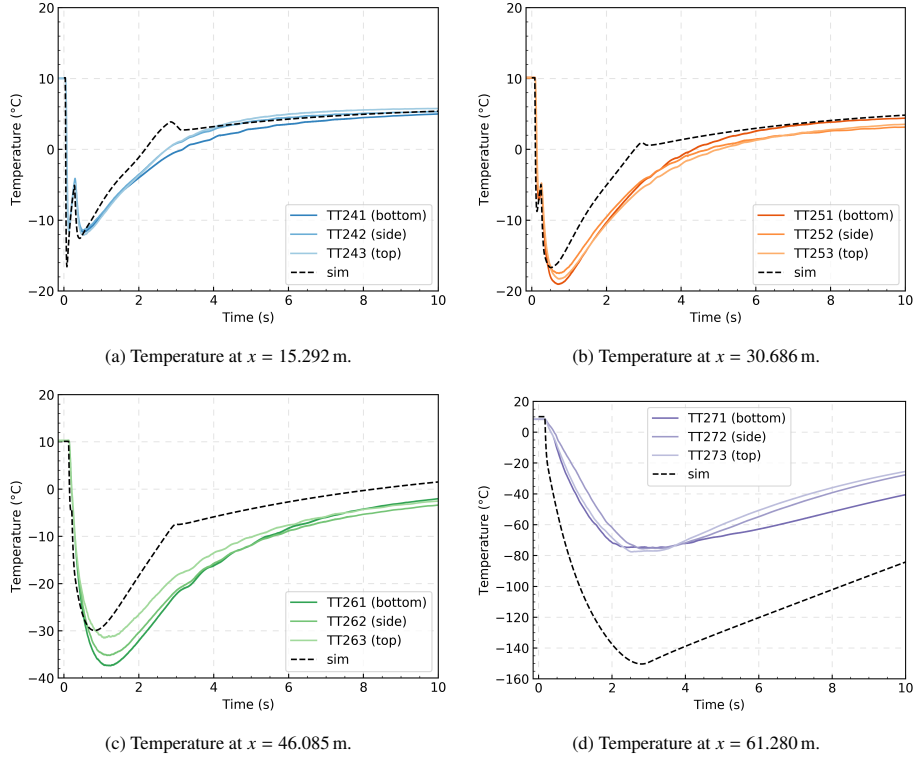
(a) Temperature at $x = 15.292$ m.

(b) Temperature at $x = 30.686$ m.

(c) Temperature at $x = 46.085$ m.

(d) Temperature at $x = 61.280$ m.

Figure 16: Measured and simulated temperature for Test no. 11.

We now consider Test no. 6 for pure CO_2 with an initial state of 10.4 MPa and 40.0 °C. Figure 17 displays measured and simulated temperature as a function of time for different positions, whereas Figure 18 shows temperature profiles along the pipe for different times. Figure 17a shows the temperature at a position 8 cm from the outlet. First, we observe that the temperature sensors appear to be fast enough to capture the initial rapid cooling. Next, at about 3.25 s, the measured temperature starts rising. That is, this is the dry-out point, at which the last liquid has evaporated. The HEM predicts dry-out about half a second earlier, thus underestimating the temperature drop. This is consistent with the assumptions inherent in the HEM. Since the model has no slip between the phases, we expect it to predict too large an outflow of liquid and hence earlier dry-out. Overall, however, the agreement between the measured and simulated temperatures is good at this point, indicating a highly dispersed flow not too far from the assumption in the HEM.

Figures 17b and 17c show the temperatures recorded at about 15 m from the outlet and from the closed end, respectively. At these axial positions, we have three temperature sensors, oriented close to the top, bottom and side of the tube, see Figure 5. Before about 4 s, we observe that the sensors give the same temperature. This indicates a highly dispersed two-phase flow. After this time, the sensor readings starts deviating, indicating stratification of the flow. Solid CO_2 could also be formed, as the triple-point pressure is reached at this point. We interpret the somewhat jagged signals as stemming from drops or slugs hitting the sensors. We observe that dry-out occurs later at the farther position (Figure 17c), and a larger difference between the sensors at this

19

(a) Temperature at $x = 0.080$ m.

(b) Temperature at $x = 15.292$ m.

(c) Temperature at $x = 46.085$ m.

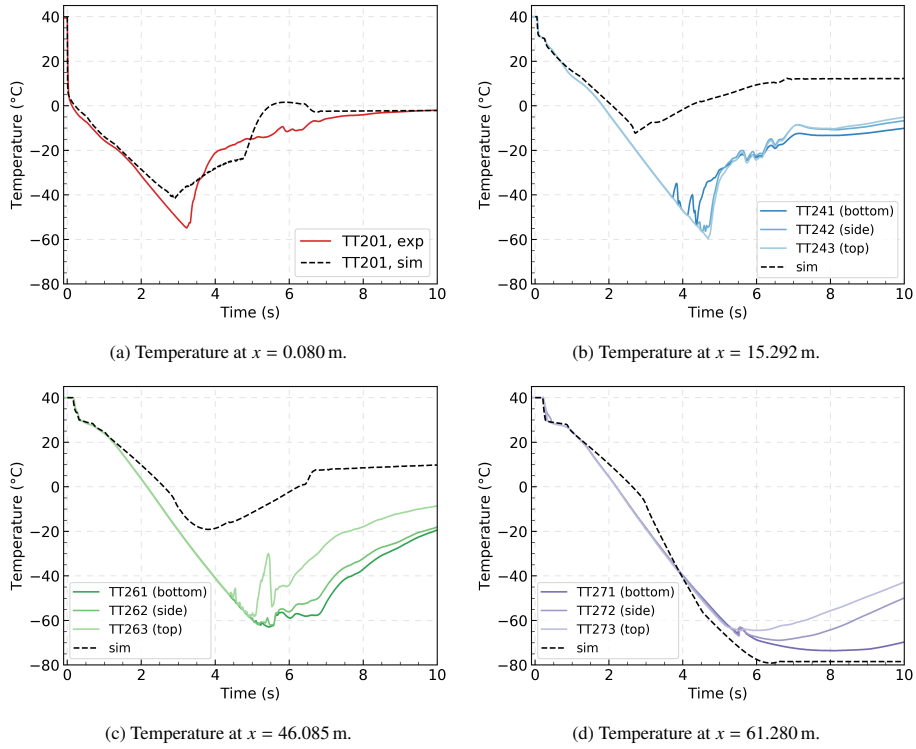(d) Temperature at $x = 61.280$ m.

Figure 17: Measured and simulated temperature for Test no. 6.
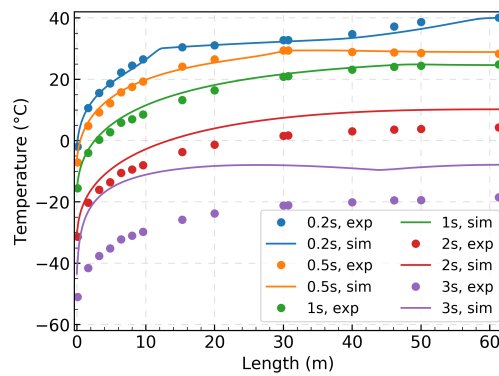
Figure 18: Measured (dots) and simulated (full lines) temperature along the pipe for Test no. 6.

(a) Temperature at $x = 0.080$ m.

(b) Temperature at $x = 15.292$ m.

(c) Temperature at $x = 46.085$ m.

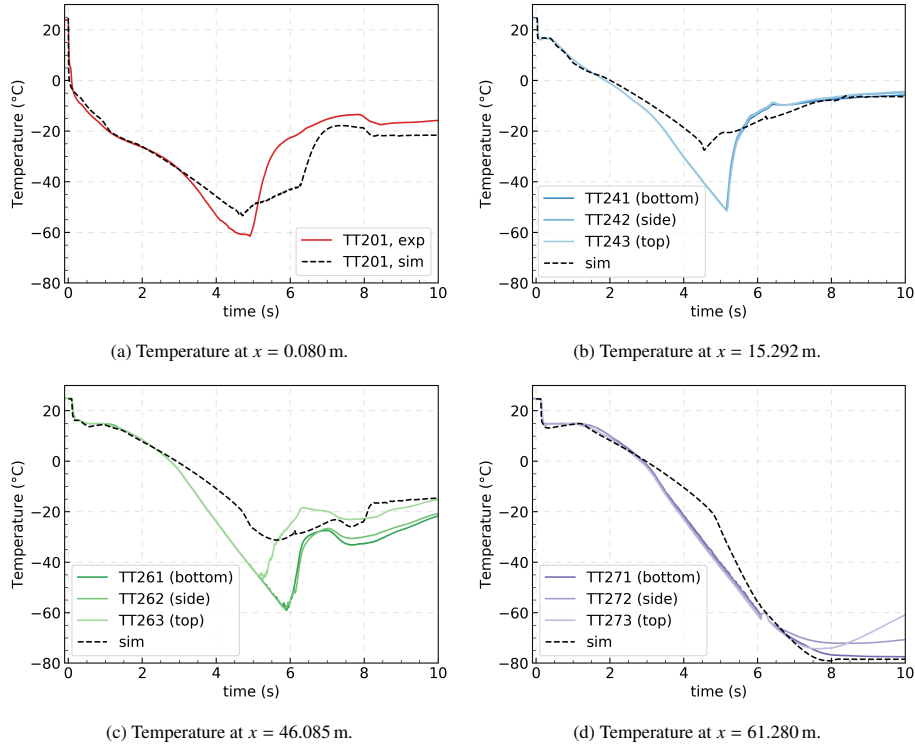(d) Temperature at $x = 61.280$ m.

Figure 19: Measured and simulated temperature for Test no. 8.

point may indicate a larger degree of flow stratification.

The trend at the closed end of the tube is different, as seen in Figure 17d. Here the agreement between the model and the measurements is good, at least until about 6 s, despite the fact that we would expect gas-liquid stratification. This is related to the formation of solid CO_2, which is accounted for in our HEM. In the measurements, this can, in our interpretation, be observed at the kink in the trend at about 5.5 s. After this point, we observe a stratification in the measured temperature, presumably due to some solid CO_2 remaining at the bottom of the tube, with the coldest temperature attaining nearly -80 °C.

The measured and simulated temperatures for Test no. 8, with an initial state of 12.22 MPa and 24.6 °C, are displayed in Figures 19 and 20, which can be compared with Figures 17 and 18 for Test no. 6. We observe that for Test no. 8, the temperatures calculated by the HEM are in better agreement with the measurements than for Test no. 6. This may be explained by the following observations. First, due to the initial state, for a given pressure, Test no. 6 will have a larger gas fraction than Test no. 8. This has as an effect that dry-out at the outlet occurs at about 3.2 s in Test no. 6 (Figure 17a) and later, at about 5 s, in Test no. 8 (Figure 19a). In the middle of the tube, on the other hand, dry-out occurs at about the same time, i.e., at 6 s for Test no. 8 (Figure 19c) compared to 5.5 s for Test no. 6 (Figure 17c). We also observe that the difference between the predicted dry-out time and the measured dry-out time is significantly smaller for Test no. 8 (Figure 19) than for Test no. 6 (Figure 17). This indicates that in Test no. 6, the phase slip is higher, i.e., further from the no-slip assumption in the HEM.
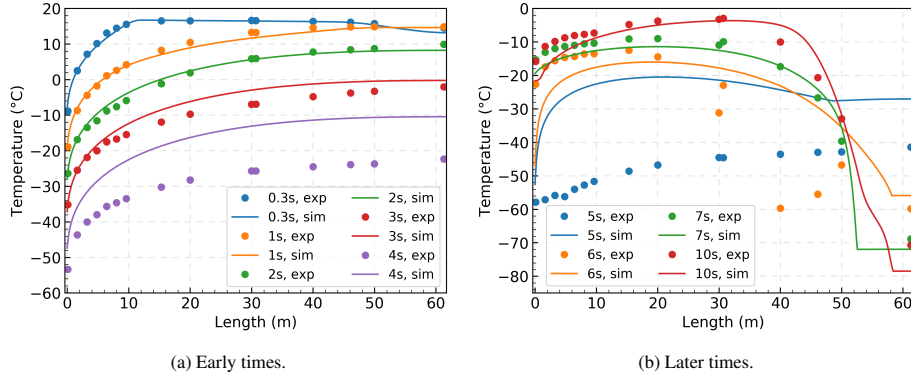
21

(a) Early times.

(b) Later times.

Figure 20: Measured (dots) and simulated (full lines) temperature along the pipe for Test no. 8.

5. Conclusion

The design and operation of CO_2 transportation and injection systems will benefit from transient flow models handling multiple phases (gas, liquid, solid) in order to reduce cost while maintaining safety. The development and validation of such models hinge on accurate experimental data with high resolution in space and time. In this paper, we have presented a new experimental facility constructed to provide such data for the depressurization of a tube filled with CO_2 or CO_2-rich mixtures. A series of full-bore depressurization experiments has been conducted with pure N_2 and CO_2, and they have been compared to calculations with a homogeneous equilibrium model in order to check data consistency and provide a reference for discussion. We make the following observations from the experiments:

1. In all the conducted experiments with CO_2, phase transition occurred. This entailed a higher complexity in the observed phenomena and larger challenges in their modelling than what was the case for N_2.
2. Even a case initially in a gaseous phase (Test 3) yielded phase transition during decompression.
3. For initial pressures around $10\,\mathrm{MPa}$ (Tests 6 and 8), a lower initial temperature yields a denser state with lower compressibility and a significantly faster decompression. This in turn yields a boiling pressure below that predicted assuming thermodynamic equilibrium. Indeed, we observed a behaviour lying between that calculated assuming equilibrium and that calculated for a meta-stable liquid. This is relevant, among other things, for the prediction of running-ductile fracture in CO_2-transportation pipelines, and it should be addressed by future modelling work.
4. For the depressurization of CO_2 from a gaseous state (Test 3), the observed decompression-wave speed indicated the formation of liquid drops at a pressure lower than that predicted assuming full equilibrium.
5. The observed single-phase decompression-wave speeds corresponded very well with those calculated using the Span–Wagner EOS and the decompression relation (3). Calculations assuming full equilibrium were in fair agreement with observed two-phase decompression-wave speeds. This indicates the occurrence of a highly dispersed flow.

6. The temperature observations at the closed end of the tube indicated the formation of solid CO_2 during the experiments starting from a dense liquid state, i.e., Tests 6 and 8.

7. For the dense-phase experiments, the temperature observations indicated a stratification of the flow somewhat before dry-out.

8. The dry-out point can be observed as the time, for a given location, at which the temperature starts rising after the initial cooling. The HEM predicted dry-out earlier than the experimental observations. This is expected due to the fact that there is no phase slip in the HEM. Thus it would predict too much liquid leaving the tube and hence early dry-out.

9. The HEM gave good temperature predictions close to the outlet. This indicates that a highly dispersed flow pattern is a fair assumption at that point. The HEM also gave good temperature predictions at the closed end of the tube. This could indicate that the phase equilibrium dominates the temperature evolution there. The deviation was largest in the middle of the tube. We hypothesize that better prediction may be obtained by including phase slip and refined heat-transfer models.

10. The present experimental observations should be employed in future modelling work.

Acknowledgements

Data availability

The experimental data recorded in this study can be downloaded from Zenodo (Munkejord *et al.*, 2020).

References

Armstrong, K., Allason, D., Oct. 2014. *2″ NB shocktube releases of dense phase CO₂*. Tech. rep., GL Noble Denton, Gilsland Cumbria, UK. URL https://www.dnvgl.com/oilgas/innovation-development/joint-industry-projects/co2pipetrans.html.

Aursand, E., Dumoulin, S., Hammer, M., Lange, H. I., Morin, A., Munkejord, S. T., Nordhagen, H. O., Sep. 2016a. Fracture propagation control in CO_2 pipelines: Validation of a coupled fluid-structure model. *Eng. Struct.* 123, 192–212. doi:10.1016/j.engstruct.2016.05.012.

Aursand, P., Gjennestad, M. A., Aursand, E., Hammer, M., Wilhelmsen, Ø., 2016b. The spinodal of single- and multi-component fluids and its role in the development of modern equations of state. *Fluid Phase Equilib.* 436, 98–112. doi:10.1016/j.fluid.2016.12.018.

Aursand, P., Hammer, M., Lavrov, A., Lund, H., Munkejord, S. T., Torsæter, M., Jul. 2017. Well integrity for CO_2 injection from ships: Simulation of the effect of flow and material parameters on thermal stresses. *Int. J. Greenh. Gas Con.* 62, 130–141. doi:10.1016/j.ijggc.2017.04.007.

Bejan, A., 1993. *Heat Transfer*. John Wiley & Sons, Inc., New York. ISBN 0-471-50290-1.

Botros, K. K., Dec. 2010. Measurements of speed of sound in lean and rich natural gas mixtures at pressures up to 37 MPa using a specialized rupture tube. *Int. J. Thermophys.* 31 (11–12), 2086–2102. doi:10.1007/s10765-010-0888-4.

Botros, K. K., Geerligs, J., Rothwell, B., Carlson, L., Fletcher, L., Venton, P., Dec. 2010. Transferability of decompression wave speed measured by a small-diameter shock tube to full size pipelines and implications for determining required fracture propagation resistance. *Int. J. Pres. Ves. Pip.* 87 (12), 681–695. doi:10.1016/j.ijpvp.2010.10.006.

Botros, K. K., Geerligs, J., Rothwell, B., Robinson, T., Jun. 2016. Measurements of decompression wave speed in pure carbon dioxide and comparison with predictions by equation of state. *J. Press. Vess. – T. ASME* 138 (3). doi:10.1115/1.4031941.

Botros, K. K., Geerligs, J., Rothwell, B., Robinson, T., Mar. 2017a. Effect of argon as the primary impurity in anthropogenic carbon dioxide mixtures on the decompression wave speed. *Can. J. Chem. Eng.* 95 (3), 440–448. doi:10.1002/cjce.22689.

Botros, K. K., Geerligs, J., Rothwell, B., Robinson, T., Apr. 2017b. Measurements of decompression wave speed in binary mixtures of carbon dioxide mixtures and impurities. *J. Press. Vess. – T. ASME* 139 (2). doi:10.1115/1.4034016.

Botros, K. K., Geerligs, J., Rothwell, B., Robinson, T., Apr. 2017c. Measurements of decompression wave speed in simulated anthropogenic carbon dioxide mixtures containing hydrogen. *J. Press. Vess. – T. ASME* 139 (2). doi:10.1115/1.4034466.

Botros, K. K., Geerligs, J., Zhou, J., Glover, A., Jun. 2007. Measurements of flow parameters and decompression wave speed following rupture of rich gas pipelines, and comparison with GASDECOM. *Int. J. Pres. Ves. Pip.* 84 (6), 358–367. doi:10.1016/j.ijpvp.2007.01.005.

Botros, K. K., Hippert, E., Jr., Craidy, P., Jun. 2013. Measuring decompression wave speed in CO_2 mixtures by a shock tube. *Pipelines International* 16, 22–28.

Botros, K. K., Studzinski, W., Geerligs, J., Glover, A., 2004. Determination of decompression wave speed in rich gas mixtures. *Can. J. Chem. Eng.* 82 (5), 880–891. doi:10.1002/cjce.5450820503.

Brown, S., Martynov, S., Mahgerefteh, H., Chen, S., Zhang, Y., 2014. Modelling the non-equilibrium two-phase flow during depressurisation of CO_2 pipelines. *Int. J. Greenh. Gas Con.* 30, 9–18. doi:10.1016/j.ijggc.2014.08.013.

Brown, S., Martynov, S., Mahgerefteh, H., Proust, C., 2013. A homogeneous relaxation flow model for the full bore rupture of dense phase CO_2 pipelines. *Int. J. Greenh. Gas Con.* 17, 349–356. doi:10.1016/j.ijggc.2013.05.020.

Cao, Q., Yan, X., Guo, X., Zhu, H., Liu, S., Yu, J., Jul. 2018. Temperature evolution and heat transfer during the release of CO_2 from a large-scale pipeline. *Int. J. Greenh. Gas Con.* 74, 40–48. doi:10.1016/j.ijggc.2018.04.015.

Clausen, S., Oosterkamp, A., Strøm, K. L., 2012. Depressurization of a 50 km long 24 inches CO_2 pipeline. In: Røkke, N. A., Hägg, M.-B., Mazzetti, M. J. (Eds.), *6th Trondheim Conference on CO_2 Capture, Transport and Storage (TCCS-6)*. BIGCCS / SINTEF / NTNU, Energy Procedia vol. 23, Trondheim, Norway, pp. 256–265. doi:10.1016/j.egypro.2012.06.044.

Cosham, A., Jones, D. G., Armstrong, K., Allason, D., Barnett, J., 24–28 Sep 2012a. The decompression behaviour of carbon dioxide in the dense phase. In: *9th International Pipeline Conference, IPC2012*. ASME, IPTI, Calgary, Canada, vol. 3, pp. 447–464. doi:10.1115/IPC2012-90461.

Cosham, A., Jones, D. G., Armstrong, K., Allason, D., Barnett, J., 24–28 Sep 2012b. Ruptures in gas pipelines, liquid pipelines and dense phase carbon dioxide pipelines. In: *9th International Pipeline Conference, IPC2012*. ASME, IPTI, Calgary, Canada, vol. 3, pp. 465–482. doi:10.1115/IPC2012-90463.

Cosham, A., Jones, D. G., Armstrong, K., Allason, D., Barnett, J., 29 Sep–3 Oct 2014. Analysis of two dense phase carbon dioxide full-scale fracture propagation tests. In: *10th International Pipeline Conference, IPC2014*. Calgary, Canada, vol. 3. doi:10.1115/IPC2014-33080.

Cosham, A., Jones, D. G., Armstrong, K., Allason, D., Barnett, J., 26–30 Sep 2016. Analysis of a dense phase carbon dioxide full-scale fracture propagation test. In: *11th International Pipeline Conference, IPC2016*. Calgary, Canada, vol. 3. doi:10.1115/IPC2016-64456.

Di Biagio, M., Lucci, A., Mecozzi, E., Spinelli, C. M., May 2017. Fracture propagation prevention on CO_2 pipelines: Full scale experimental testing and verification approach. In: *12th Pipeline Technology Conference*. Lab. Soete and Tiratsoo Technical, Berlin, Germany. Paper no. S06-02.

DNV, Aug. 2012. Submarine pipeline systems. Offshore standard DNV-OS-F-101.

Drescher, M., Varholm, K., Munkejord, S. T., Hammer, M., Held, R., de Koeijer, G., Oct. 2014. Experiments and modelling of two-phase transient flow during pipeline depressurization of CO_2 with various N_2 compositions. In: Dixon, T., Herzog, H., Twinning, S. (Eds.), *GHGT-12 – 12th International Conference on Greenhouse Gas Control Technologies*. University of Texas at Austin / IEAGHGT, Energy Procedia, vol. 63, Austin, Texas, USA, pp. 2448–2457. doi:10.1016/j.egypro.2014.11.267.

ECCSEL, 2020. Depressurization facility. `https://www.eccsel.org/facilities/transport/no25_sintef_er_depress/`. Accessed 2020-03-31.

Edenhofer, O., Pichs-Madruga, R., Sokona, Y., Farahani, E., Kadner, S., Seyboth, K., Adler, A., Baum, I., Brunner, S., Eickemeier, P., Kriemann, B., Savolainen, J., Schlømer, S., von Stechow, C., Zwickel, T., (eds.), J. M., 2014. *Climate Change*

2014: Mitigation of Climate Change. Tech. rep., Working Group III Contribution to the Fifth Assessment Report of the Intergovernmental Panel on Climate Change, Summary for Policymakers, IPCC. URL `http://mitigation2014.org/`.

Friedel, L., Jun. 1979. Improved friction pressure drop correlations for horizontal and vertical two phase pipe flow. In: *Proceedings, European Two Phase Flow Group Meeting*. Ispra, Italy. Paper E2.

Gu, S., Li, Y., Teng, L., Wang, C., Hu, Q., Zhang, D., Ye, X., Wang, J., Iglauer, S., May 2019. An experimental study on the flow characteristics during the leakage of high pressure CO_2 pipelines. *Process Saf. Environ.* 125, 92–101. doi:10.1016/j.psep.2019.03.010.

Gungor, K. E., Winterton, R. H. S., Mar. 1987. Simplified general correlation for saturated flow boiling and comparisons of correlations with data. *Chem. Eng. Res. Des.* 65 (2), 148–156.

Guo, X., Yan, X., Yu, J., Yang, Y., Zhang, Y., Chen, S., Mahgerefteh, H., Martynov, S., Collard, A., Jan. 2017. Pressure responses and phase transitions during the release of high pressure CO_2 from a large-scale pipeline. *Energy* 118, 1066–1078. doi:10.1016/j.energy.2016.10.133.

Guo, X., Yan, X., Yu, J., Zhang, Y., Chen, S., Mahgerefteh, H., Martynov, S., Collard, A., Proust, C., Sep. 2016. Pressure response and phase transition in supercritical CO_2 releases from a large-scale pipeline. *Appl. Energ.* 178, 189–197. doi:10.1016/j.apenergy.2016.06.026.

Hammer, M., Ervik, Å., Munkejord, S. T., 2013. Method using a density-energy state function with a reference equation of state for fluid-dynamics simulation of vapor-liquid-solid carbon dioxide. *Ind. Eng. Chem. Res.* 52 (29), 9965–9978. doi:10.1021/ie303516m.

IEA, 2017. *Energy Technology Perspectives.* ISBN 978-92-64-27597-3. doi:10.1787/energy_tech-2017-en.

Jie, H. E., Xu, B. P., Wen, J. X., Cooper, R., Barnett, J., Sep. 2012. Predicting the decompression characteristics of carbon dioxide using computational fluid dynamics. In: *9th International Pipeline Conference IPC2012*. ASME, IPTI, Calgary, Canada, pp. 585–595. doi:10.1115/IPC2012-90649.

Joint Committee for Guides in Metrology, Sep. 2008. Evaluation of measurement data – Guide to the expression of uncertainty in measurement. JCGM 100:2008. URL `https://www.bipm.org/utils/common/documents/jcgm/JCGM_100_2008_E.pdf`.

Jones, D. G., Cosham, A., Armstrong, K., Barnett, J., Cooper, R., Oct. 2013. Fracture-propagation control in dense-phase CO_2 pipelines. In: *6th International Pipeline Technology Conference*. Lab. Soete and Tiratsoo Technical, Ostend, Belgium. Paper no. S06-02.

Maxey, W. A., Nov. 1974. Fracture initiation, propagation and arrest. In: *Fifth Symposium on Line Pipe Research*. American Gas Association, Houston, Texas, USA, pp. J1–J31.

Michal, G., Davis, B., Østby, E., Lu, C., Røneid, S., Sep. 2018. CO2SAFE-ARREST: A full-scale burst test research program for carbon dioxide pipelines – Part 2: Is the BTCM out of touch with dense-phase CO_2? In: *12th International Pipeline Conference, IPC 2018*. ASME. doi:10.1115/IPC2018-78525.

Munkejord, S. T., Austegard, A., Deng, H., Hammer, M., Stang, H. G. J., Løvseth, S. W., 2020. Depressurization of CO_2 in a pipe: High-resolution pressure and temperature data and comparison with model predictions – dataset. Zenodo. doi:10.5281/zenodo.3928227.

Munkejord, S. T., Hammer, M., Jun. 2015. Depressurization of CO_2-rich mixtures in pipes: Two-phase flow modelling and comparison with experiments. *Int. J. Greenh. Gas Con.* 37, 398–411. doi:10.1016/j.ijggc.2015.03.029.

Munkejord, S. T., Hammer, M., Løvseth, S. W., May 2016. CO_2 transport: Data and models – A review. *Appl. Energ.* 169, 499–523. doi:10.1016/j.apenergy.2016.01.100.

Peng, D. Y., Robinson, D. B., Feb. 1976. A new two-constant equation of state. *Ind. Eng. Chem. Fund.* 15 (1), 59–64. doi:10.1021/i160057a011.

Pham, L. H. H. P., Rusli, R., 2016. A review of experimental and modelling methods for accidental release behaviour of high-pressurised CO_2 pipelines at atmospheric environment. *Process Saf. Environ.* 104, 48–84. doi:10.1016/j.psep.2016.08.013.

Span, R., Wagner, W., Nov.–Dec. 1996. A new equation of state for carbon dioxide covering the fluid region from the triple-point temperature to 1100 K at pressures up to 800 MPa. *J. Phys. Chem. Ref. Data* 25 (6), 1509–1596. doi:10.1063/1.555991.

Taylor, B. N., Kuyatt, C. E., Sep. 1994. *Guidelines for evaluating and expressing the uncertainty of NIST measurement results*. Technical Note 1297, National Institute of Standards and Technology, Gaithersburg, Maryland, USA. URL `https://nvlpubs.nist.gov/nistpubs/Legacy/TN/nbstechnicalnote1297.pdf`.

Teng, L., Li, Y., Zhao, Q., Wang, W., Hu, Q., Ye, X., Zhang, D., Nov. 2016. Decompression characteristics of CO_2 pipelines following rupture. *J. Nat. Gas Sci. Eng.* 36 (A), 213–223. doi:10.1016/j.jngse.2016.10.026.

Toro, E. F., Billett, S. J., Nov. 2000. Centred TVD schemes for hyperbolic conservation laws. *IMA J. Numer. Anal.* 20 (1), 47–79. doi:10.1093/imanum/20.1.47.

Voldsund, M., Gardarsdottir, S., De Lena, E., Pérez-Calvo, J.-F., Jamali, A., Berstad, D., Fu, C., Romano, M., Roussanaly, S., Anantharaman, R., Hoppe, H., Sutter, D., Mazzotti, M., Gazzani, M., Cinti, G., Jordal, K., 2019. Comparison of technologies for CO_2 capture from cement production – Part 1: Technical evaluation. *Energies* 12 (3), 559. doi:10.3390/en12030559.

Wilhelmsen, Ø., Aasen, A., Skaugen, G., Aursand, P., Austegard, A., Aursand, E., Gjennestad, M. A., Lund, H., Linga, G., Hammer, M., 2017. Thermodynamic Modeling with Equations of State: Present Challenges with Established Methods. *Ind. Eng. Chem. Res.* 56 (13), 3503–3515. doi:10.1021/acs.iecr.7b00317.

Yan, X., Guo, X., Yu, J., Chen, S., Zhang, Y., Mahgerefteh, H., Martynov, S., Brown, S., 2018. Flow characteristics and dispersion during the vertical anthropogenic venting of supercritical CO_2 from an industrial scale pipeline. In: Yan, J., Feitz, A., Li, X., Zhang, X. (Eds.), *Applied Energy Symposium and Forum, Carbon Capture, Utilization and Storage, CCUS 2018*. Energy Procedia, vol. 154, Perth, Australia, pp. 66–72. doi:10.1016/j.egypro.2018.11.012.